Pore, live root and necromass quantification in complex heterogeneous wetland soils using X-ray computed tomography

Clementine Chirol [a,*], Simon J. Carr [a,b], Kate L. Spencer [a], Iris Moeller [a,c]

[a] School of Geography, Queen Mary University London, Mile End Road, E1 4NS London, UK
[b] University of Cumbria, Institute of Science, Natural Resources and Outdoor Studies, LA22 9BB Ambleside, Cumbria, UK
[c] Trinity College Dublin, School of Geography, Dublin 2, Ireland

ARTICLE INFO

ABSTRACT

Subsurface structures and especially the interactions between pores, roots and other organic matter elements have a strong impact on ecosystem functioning. Yet despite recent progress in the application of X-ray Computed Microtomography (μCT) to soil structure in agricultural science, applications to the more complex and heterogeneous substrates found in natural soils, specifically wetland soils, remain sparse. We apply X-ray μCT to a complex heterogenous soil and develop a robust segmentation method to quantify the pores, live roots and necromass. This approach significantly improves the detection of the organic matter elements, and gives us unprecedented detail and resolution in the segmentation of pores, live roots and necromass at a high spatial resolution (62.5 μm in this study). We identify several situations where pores and organic matter interact in the soil, including the disconnected air spaces (aerenchyma) that run within the *Spartina* stem and roots, tubular-shaped pores left behind by decaying roots, and lateral roots deploying within structural fragilities in the sediment. The capacity of X-ray μCT to distinguish the connected live root system from the necromass opens possibilities for applications to determine key wetland soil functions such as soil cohesivity, soil nutrient exchanges and soil carbon dynamics.

1. Introduction

Soils and sediments, formed respectively from the in-situ weathering of a bedrock in association with biogeochemical processes (Lin, 2010) and from the layered deposition of imported particles (Dyer, 1995), both play a critical role for the ecosystems they support. They are a place of exchange of water, gases and other resources, while providing structural support and shelter for dwelling organisms (Rabot et al., 2018). The structure of these subsurface environments, defined as the three-dimensional spatial arrangement of solids regardless of chemical heterogeneity (Rabot et al., 2018; Xiong et al., 2019), results from the unique pedological (soil) and hydrodynamic (sediment) history of each habitat and is dynamic over multiple spatial and temporal scales. Because of this heterogeneity, structural properties (e.g. the measurable components of the soil structure, such as total porosity) are difficult to describe, yet doing so can greatly improve our understanding of ecosystem functions. Structure conditions geomorphological,

pedological and ecological functioning (Corenblit et al., 2011; Lin, 2010; Rabot et al., 2018) and soil/sediment mechanics (Fonseca et al., 2013; Keller et al., 2013; Menzies et al., 2016; Phillips et al., 2018; Spagnolo et al., 2016). Structure notably controls the soils' interactions with the surface by providing pathways for gas, water and solute fluxes (Ball, 2013; Dale et al., 2019; Gharedaghloo et al., 2018; Pedersen et al., 2015; Spencer et al., 2017; Swanson et al., 2017). Live roots also provide pathways of gas and nutrient exchanges, and play an important role in soil carbon dynamics (Bardgett et al., 2014; Blagodatsky & Smith, 2012; Smith et al., 2003). Due to these combined functions, structure exerts a critical control over soil/sediment fertility and agricultural potential (Naveed et al., 2016; Pöhlitz et al., 2018; Rogers et al., 2016).

Because of the complexity of soil and sediment structure, its influence on ecosystem processes cannot be accurately predicted by one-dimensional parameters measured from traditional methods in the field or in the lab (Bradley & Morris, 1990). 3D X-ray Computed Tomography (CT) utilizes the penetrating capacity and attenuation of X-

ray energy to image the 3D internal structure and relative densities of materials ('phases') in a non-destructive manner (Cnudde & Boone, 2013). The technique, developed for medical applications in the 1970s, soon led to the higher resolution method X-ray Computed Micro-tomography (µCT) in the 1980s and to the study of microstructures in the geological and soil sciences (Ketcham and Carlson, 2001; Ketcham, 2005; Carlson, 2006; Taina et al., 2008; Cnudde and Boone, 2013). In soil sciences, the application of µCT has largely focused on agricultural soils (Helliwell et al., 2013; Keller et al., 2013; Menon et al., 2020; Mooney, 2002; Rogers & Benfey, 2015; Wildenschild & Sheppard,

Fig. 1. Data acquisition and processing workflow. The overall processing time from scanning to obtention of output parameters is about four days on a high performance computing suite.

2013). By contrast, lacustrine, estuarine, glacial, fluvial and marine sediments and associated soils typically represent multiple sediment sources, with mixing and superposition of different minerogenic and biogenic components with variable water content (Bendle et al., 2015; Dale et al., 2019; Griggs et al., 2015; Spagnolo et al., 2016; Spencer et al., 2017; Tarplee et al., 2011; Voepel et al., 2019). This leads to significant textural and structural heterogeneities in samples, which challenges the data acquisition and analysis approaches developed for the examination of more homogenous agricultural soils. Here, we have focused on heterogeneous, tidally flooded saltmarshes which retain both sedimentary (e.g. laminations) and pedological (e.g., vegetation) features and are commonly referred to as soils. Therefore, for simplicity, we use the term soils to include also unconsolidated and/or vegetated sediments deposited in aquatic environments with minerogenic and biogenic components, as they present characteristics of both sediments and soils.

The acquisition and interpretation of µCT imagery of heterogeneous soils pose technical challenges. Firstly, such soils are often unconsolidated and saturated, and therefore easily disturbed, making recovery of 'undisturbed' samples very difficult, particularly at depth (Carr et al., 2020). Secondly, samples with significant physical heterogeneity are challenging to 'segment' into relevant phases based on X-ray attenuation coefficient alone. The segmentation process is further complicated where there is a significant component of fine-grained sediments below the spatial resolution of the scanning system (e.g. < 60 µm in this study), whereby an individual voxel in the reconstructed 3D volume represents the mean attenuation coefficient of all elements present within. The intermediate grayscale value resulting from that mix of phases is called the partial volume effect (Ketcham & Carlson, 2001); the more heterogenous and fine-grained the material, the harder it becomes to isolate key phases based on their grayscale values alone using global thresholding (Cnudde & Boone, 2013; Helliwell et al., 2013). Thirdly, most soils, particularly those formed in aquatic environments such as wetland soils, contain variable amounts of pore-water, meaning that the pore phase itself will be heterogeneous, with pores being air-filled, water-filled, and often a combination of these states. Vegetated environments such as coastal wetlands and saltmarshes also have significant heterogeneity in the belowground organic phase: the structure and 3D deployment of roots within the soil vary depending on the vegetation type. Furthermore, the roots' internal structure and density depend on their stage of decay, which complicates the differentiation of live roots, necromass and pore space.

Significant advancements have been made to address the challenge of µCT image segmentation applied to heterogenous substrates, using more sophisticated "local adaptive" image processing approaches such as gradient analysis and local-adaptive thresholding (Houston et al., 2013; Ngom et al., 2011; Pot et al., 2020; Schlüter et al., 2010; Tarplee et al., 2011). Automated root tracking algorithms have been developed to limit detection errors linked to the partial volume effect (Mairhofer et al., 2012); however, they only detect root systems connected to the surface by user-specified seed points, and might therefore miss buried root systems, which is a problem for soil carbon studies. Another approach is to detect phase elements based on their 3D shapes rather than their grayscale value, such as the tubular shape of roots using a Frangi filter (Frangi et al., 1998; Gao et al., 2019; Schulz et al., 2013). These recent root detection methods give promising results, but have so far been tested on sieved and repacked soils (Gao et al., 2019; Lucas et al., 2019), thus eliminating the structural complexity of in situ soil systems and limiting our insight into soil functions.

This study presents and evaluates a workflow for segmenting pores and organic phases in complex heterogeneous, saturated sediment such as those found in coastal saltmarshes. Our segmentation approach allows the user to quantify the interactions and complexity of both pores and organic matter elements, and to distinguish the surface-connected live roots from the necromass in order to get a complete picture of material interactions in heterogeneous soils. We will discuss the
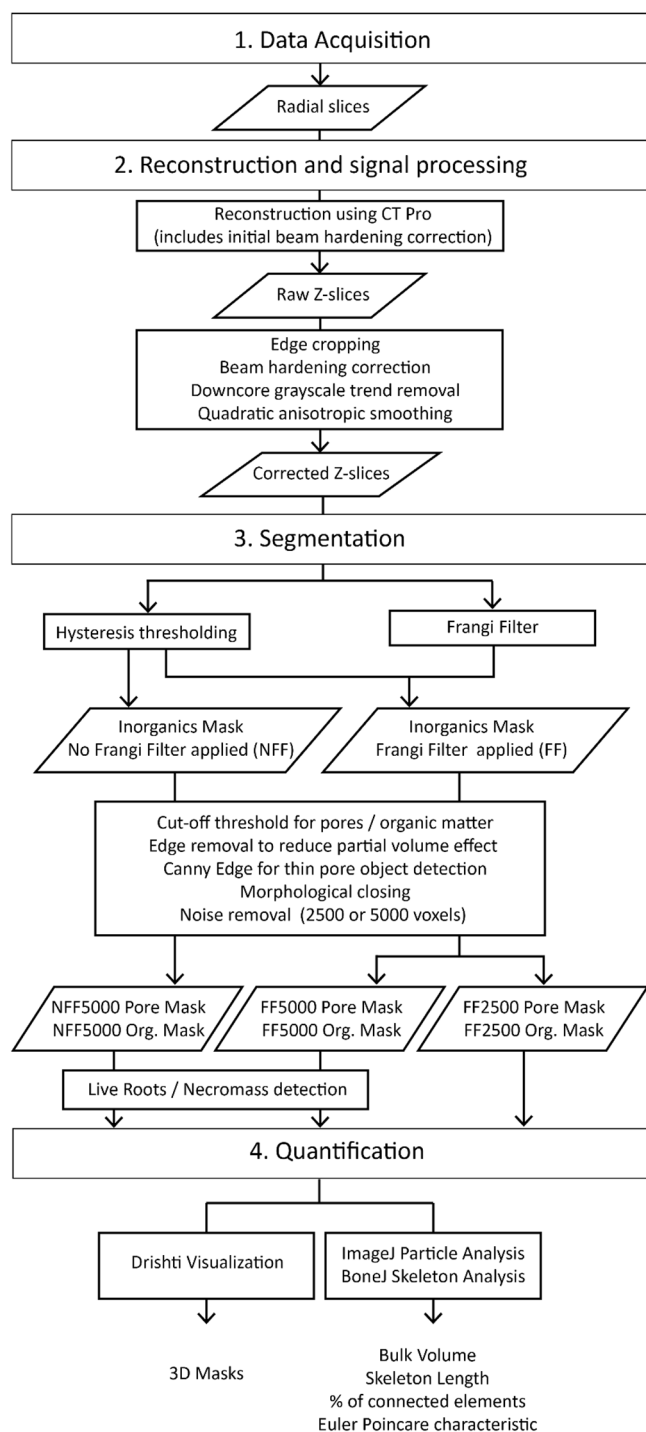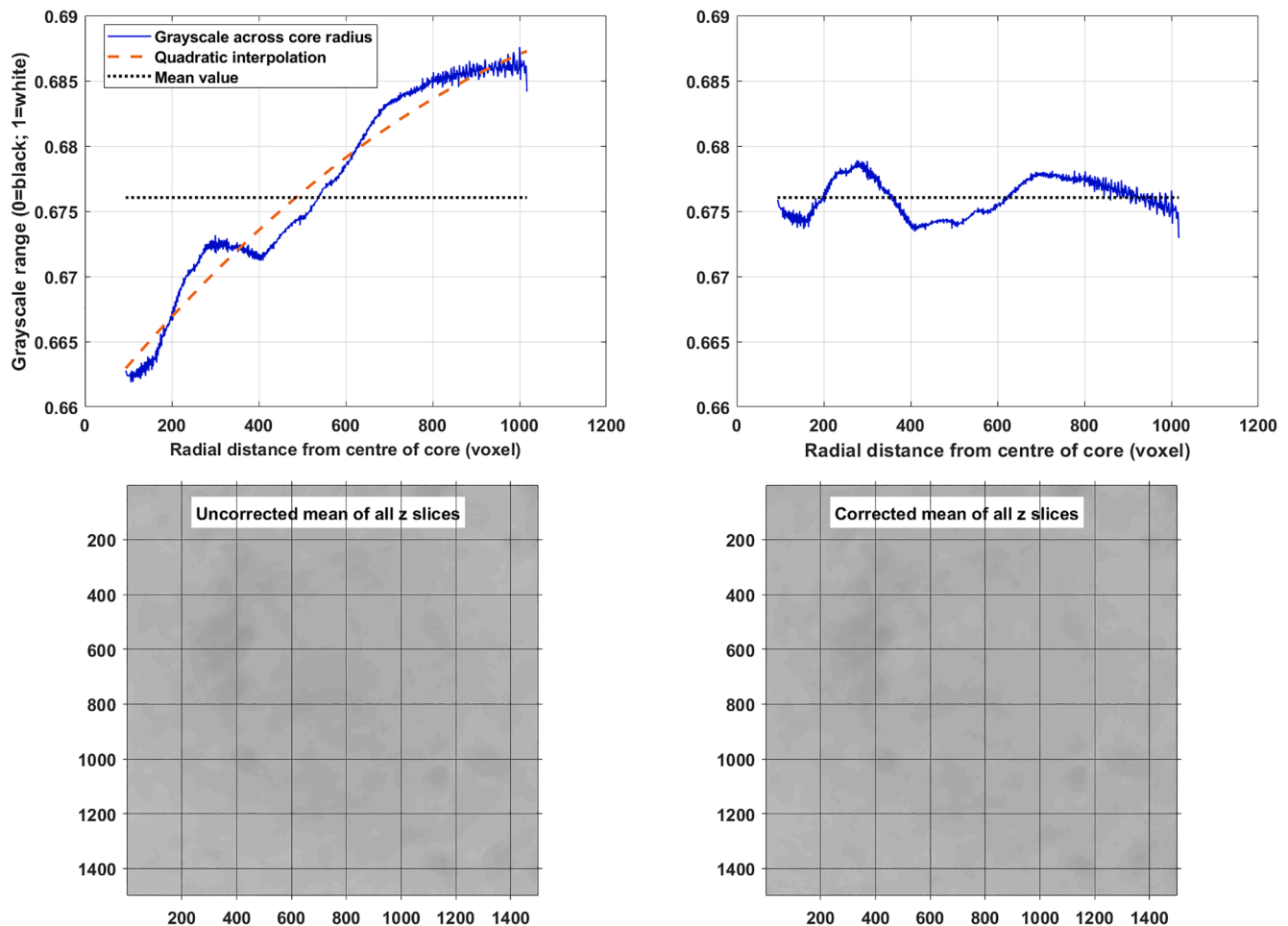
Fig. 2. Correction of the residual beam hardening using a quadratic interpolation to remove the overall trend of darker values at the center of the sample. The density variations that remain in the detrended grayscale range correspond to actual density variations in the sample.

potential applications of this approach to the study of key soil functions, such as soil–plant interactions, soil structural stability against eroding forces, and soil carbon dynamics.

2. Methods

2.1. Study site

The site chosen to conduct this study, a saltmarsh in Tillingham, Blackwater Estuary, Essex, UK, is representative of the heterogenous environments described above. Saltmarsh sediments are typically formed of mixed fine-grained sediments (clays to medium sands) and biogenic material, which makes them easily compacted and deformed during extraction. While saltmarshes have a low vegetation diversity compared to nearby non-saline environments (Teixeira et al., 2014), they are highly complex: tidal hydrology and strong vertical physico-chemical gradients mean that water content, plant survival rates, root to shoot ratio and biomass accumulation vary in space and time (Moffett et al., 2012; Pezeshki & DeLaune, 2012). In addition, the saltmarsh subsurface structure depends on tidally controlled sediment deposition, but also on post-deposition processes such as autocompaction, bio-turbation and root growth (De Battisti et al., 2019; French, 2006; Turner, 2004). These characteristics mean that saltmarsh soils are excellent candidates to test the robustness of our µCT segmentation methods on challenging, highly heterogeneous samples.

An upper saltmarsh sediment core (15 cm depth and 15 cm diameter)

was collected in July 2018. The vegetation cover at the sample location is dominated by Atriplex portulacoides (sea purslane), Puccinellia maritima and Spartina anglica (Ford et al., 2016). The sediment type is clay-dominated with a mean grain size of 69 µm, with 71% of its material below 63 µm. The sediment core was collected using the advanced trimming method initially developed by Hvorslev (1949): in brief, a plastic tube is placed on the soil surface; a trench is cut around the tube, then carved into the shape of the core while the tube is lowered around the sample, applying gentle constant pressure to limit edge drag and avoid compression and torque rotation. Large roots are cut with scissors rather than a knife to avoid jostling, impact, twisting or other defor-mation to the sediment inside the core. Fine fibrous roots are sawed through with a serrated knife to avoid crushing and displacing the sediment around them. Further details and justifications for the sam-pling method are provided by Carr et al. (2020). After extraction, the core was stored upright in a cooling box filled with bubble wrap to minimize disturbance during transport, and stored at 4 °C until required.

The core was scanned using a Nikon Metrology XT H 225 X-ray Computed Tomography (µCT) system at 205 kV and 46µA (9.4 W). The exposure time was 500 ms at 36 dB gain. A Cu 1 mm copper filter was used to reduce beam hardening artefacts. 4486 projections were ac-quired with 4 frames per projection, for a scan time of 4.5 h. The effective voxel size is 61.79 µm. The voxel grid was then downscaled to 62.5 µm during volume reconstruction. The total volume contains 2801*2783*2793 voxels. Fig. 1 summarizes the various steps applied to the scanned volume. The different steps following scanning are detailed
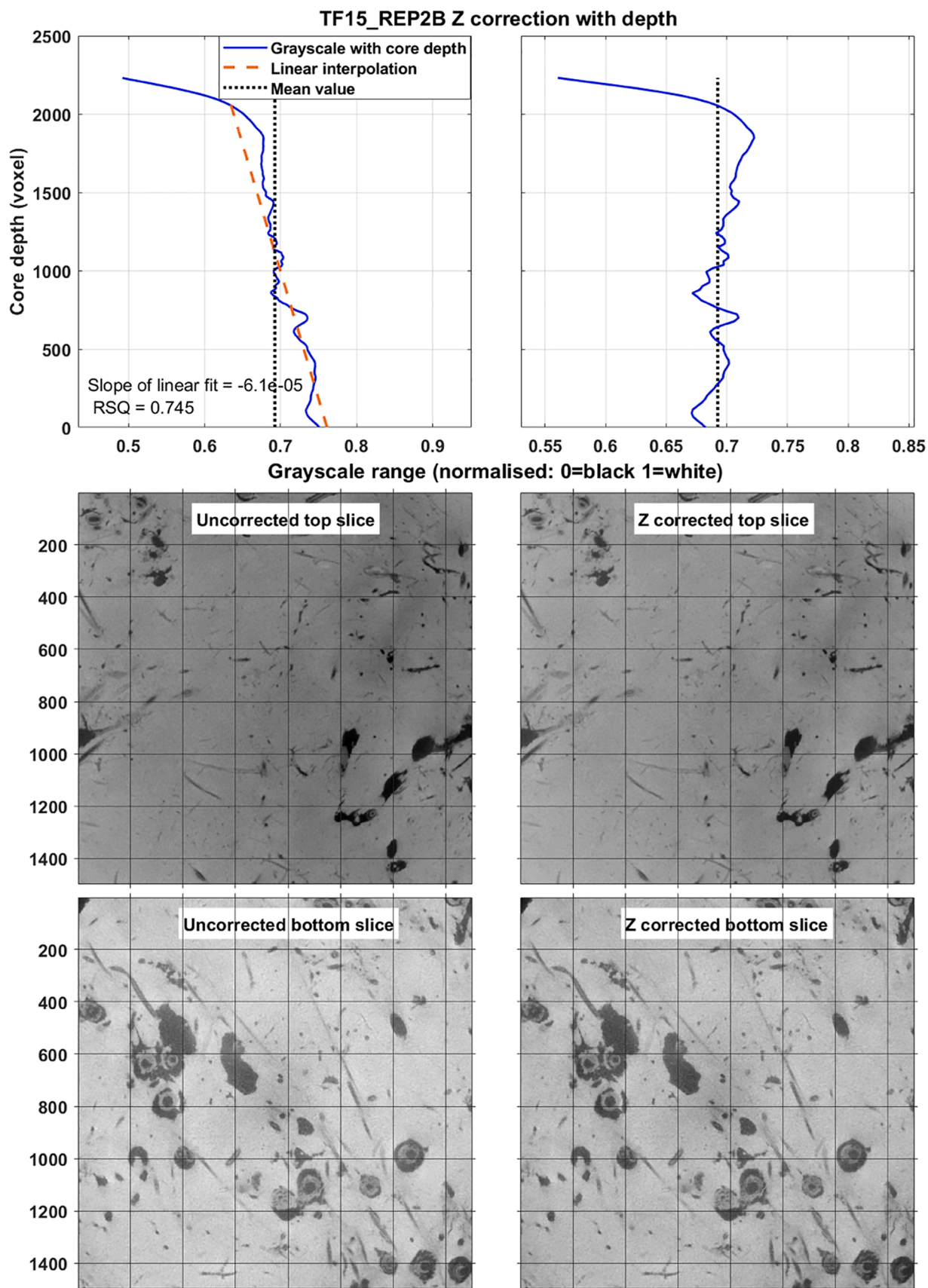
Fig. 3. Removal of the autocompaction effect on grayscales using a downcore linear fit. The correction factor at each z-slice is given by subtracting the linear fit from the uncorrected mean grayscale then adding the mean grayscale of the whole core. The method does not remove the logarithmic trend at the top of the sample so as to not excessively distort the grayscale values of the pores and organic matter.
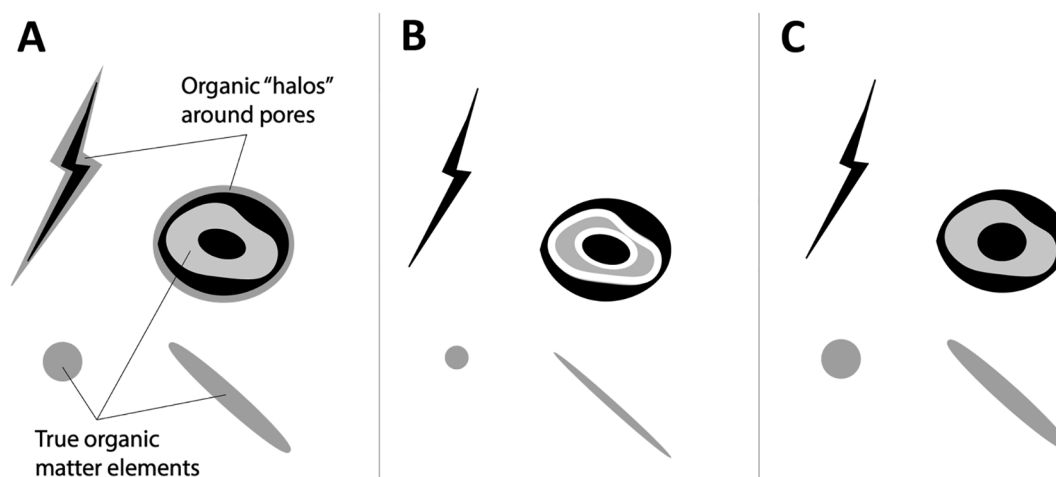
Fig. 4. Schematic diagram illustrating partial volume effect reduction using contour removal (Matlab tool *bwmorph3*) followed by dilation (Matlab tool *imdilate*). Grey: Organic matter elements. Black: Pores. A: Initial segmentation of pores and organic matter elements; the partial volume effect causes organic "halos" to be detected around the pore elements. B: Remove edges of the organic phase to erase "halos" from partial volume effect. C: Dilate remaining organic matter elements back to their original size.

in the subsections below.

2.2. Reconstruction and signal processing

The volume reconstruction step was undertaken using Nikon's in-house software CT-Pro 3D (Ray, 2011): the software finds the center of rotation of the raw X-ray projections and converts the 2D radial slices into a 3D volumetric model defined by co-registered z-slices. The software also partially corrects the z-slices for beam hardening using a polynomial fit: this imaging artefact occurs when the X-ray beam becomes progressively attenuated as it penetrates from the edge to the center of the sample, leading to an apparent darkening of the center and a brightening of the edges (Ketcham & Carlson, 2001). This type of correction works when the overall matrix can reasonably be assumed to have a consistent density throughout the sample (Ketcham & Carlson, 2001), which should be the case for our clay-dominated material. Residual beam hardening can still affect the segmentation phase, even when invisible to the naked eye. To minimize its impact while removing edge disturbances during field sampling, an 8.75*8.75 cm square mask was selected in the center of each z-slice as an area of interest and applied throughout the volume (Fig. 1). A quadratic correction was then applied to the mean radial grayscale, the grayscale value averaged vertically across the core and plotted against the radial distance from the center (Fig. 2).

Compared to other soils where the material density is consistent throughout, another challenge of clay-dominated coastal sediment is that they are highly compressible and may have rapid sedimentation rates due to material brought in by the tide (French, 2006), leading to autocompaction and to a downcore increase in the density of the inorganic phase. In our sample, a linear trend in grayscale values is found with an R^2 value of 0.75 (Fig. 3); a lack of a similar trend in the PVC tube around the sample (not shown) confirms that this trend is due to autocompaction rather than an artefact of scanning. In order to more consistently distinguish the mineral phase from the porosity and organic matter, this downcore trend is removed using a linear interpolation (Fig. 3). In practice, this means smoothing out the microporosity through the sample, which decreases with depth and affects the grayscale value of inorganic voxels due to the partial volume effect. A shift remains at the top few centimeters of the sample, where the trend is closer to a logarithmic fit in accordance with autocompaction patterns measured in silty saltmarsh clay (Bartholdy et al., 2010). However, applying a logarithmic correction to the topmost centimeters of the sample would excessively distort the grayscale value of the pores and

organic matter, which we can expect to find in greater quantity near the surface. This step improves the segmentation of pores and roots in compressible sediment and soils, which is the focus of this paper; however, analysis of the sediment phase should use the unmodified grayscale values.

Finally, in order to reduce noise in the grayscale values while preserving the edges of the pores and organic features, different smoothing algorithms were tested using image filtering tools on Matlab, including Gaussian 3D filtering, 3D median filtering, guided image filtering and anisotropic diffusion (quadratic and exponential). The quadratic anisotropic diffusion tool *imdiffusefilt* was found to be best suited for filtering out noise without losing the signal: the method enhances the contrast between matrix and darker elements by using strong gradients in the image as barriers to the smoothing effect and thus preserving the edges (Kaestner et al., 2006).

2.3. Segmentation

As stated in the introduction, μCT data applied to heterogeneous fine grained susbtrates are challenging to segment into their constituting phases because the partial volume effect blurs the limit between phases (Cnudde and Boone, 2013), and are better served by a combination of local adaptive thresholding methods. We first applied a method called hysteresis thresholding to distinguish the high-density inorganics from pores and organic matter. This method considers two thresholds: voxels below the low threshold have a high likelihood of being part of a pore or organic element and are systematically segmented, while voxels below the high threshold are only segmented if they are connected to the low threshold elements. A Frangi filter was then used to enhance tubular shapes within the sample by applying the Matlab function *FrangiFilter3D* (Kroon, 2010). The Frangi method uses the orientation patterns (eigenvalues) of the Hessian to distinguish tubular structures from plate-like or blob-like structures (Frangi et al., 1998). The output binary masks from hysteresis thresholding and Frangi tubular shape enhancement were combined, adopting a single threshold to separate pores from organic matter.

Additional steps were then added to improve the signal to noise ratio, including morphological closing and the removal of partial volume effect artefacts, which can lead to the detection of organic "halos" around pore elements. The outer edges of organic matter elements were removed, then a dilation was performed to restore the remaining organic features to their original size (Fig. 4). Finally, in the same way that root elements can have a low contrast with the surrounding inorganic matrix
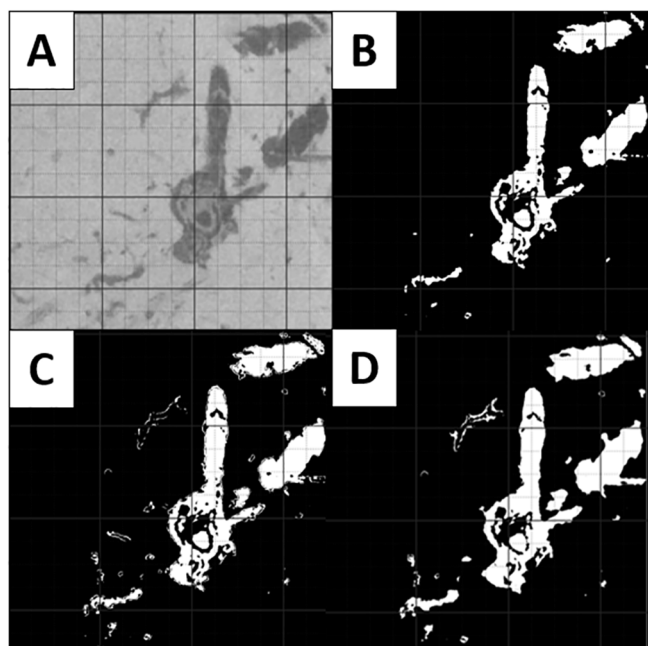
Fig. 5. Application of a Canny edge filter to refine pore detection in the sample. A: Original grayscale values. B: Pore segmentation without the Canny edge detection. C: Canny edge detection applied to find the edges of pore elements (Young, 2014); notice how the canny edges do not always connect with the features from B and add internal complexity to the pore phase. D: Morphological closing applied to reconnect the pore features to their edges (Matlab tool *imclose*).

but a characteristic tubular shape, thin cracks in the sediment can have an intermediate grayscale value due to the partial volume effect, but a visible jagged edge. To capture these remaining pore elements, we used a canny edge detection that detects both strong edges and weak edges connected to strong edges (Canny, 1986) (Fig. 5).

In order to remove the noise detected by these various methods, we tested two noise thresholds: 2,500 voxels (0.61 mm^3) and 5,000 voxels (1.22 mm^3) (FF2500 and FF5000 respectively). FF2500 contains 7,066 organic matter elements compared to 4,106 for FF5000 according to the Matlab volumetric image processing function *bwconncomp*; this will significantly increase the computational intensity of the quantification phase. Through visual comparison of the 3D volumes for FF5000 and FF2500, and quantitative comparison of the percentages of pore and organic fractions with depth, we tested whether this lower threshold significantly improves signal detection, or whether the additional ~ 3,000 elements detected are noise elements with little impact on the structure of the organic matter phase. We also tested whether the application of a Frangi filter, which takes several hours to run, significantly changes the detection of the live roots and necromass. To that end, a third version of the dataset NFF5000 was produced, using all the previous steps except for the Frangi filter, and using a noise removal threshold of 5,000 voxels.

Traditional methods for distinguishing live from dead roots are based on color, shape and plasticity (Persson, 2012). However, color and plasticity are not visible in μCT images, and while live roots tend to be larger and better branched than dead roots, densely grouped dead roots may be detected as one large, complex connected system; using these traditional definitions would therefore be prone to errors. Instead, in the binary masks NFF5000 and FF5000, we defined the live root system as all elements connected to the surface layer, approximated by the top 80 voxels (=5mm) of the sample. The remaining, unconnected elements were classified as necromass.

Table 1
List of morphological parameters considered.

Parameter	Unit	Definition
Total phase fraction	%	Fraction of the number of voxels belonging to a phase by the total number of voxels in each Z-slice and represented as depth profiles. The surface of the sample is automatically detected as the Z-slice wherein the proportion of matrix to void, segmented using an Otsu global thresholding, first reaches 75%.
Total volume	mm3	Total volume of the studied phase
Total skeleton length	mm	Total length of the skeleton, obtained by shrinking a volume to a 1-voxel thick median structure, composed of nodes and branches that preserve the topological complexity of the initial volume.
Connectedness	%	Volume of the largest connected element divided by the total volume of the studied phase
Maximum Euler-Poincare characteristic	No unit	Topological invariant that describes the shape or structure of a topological space. In BoneJ, it is calculated as the number of objects minus the number of handles (hole that goes through an object) plus the number of cavities (holes enclosed within the object). It is used as a proxy for complexity and connectedness: negative values correspond to a well-connected complex system.

2.4. Quantification and ground referencing

The 3D binary masks NFF5000, FF5000 and FF2500 were used for a detailed topological analysis of the pores and organic matter elements using the automated software plugin BoneJ for ImageJ (Doube et al., 2010; Schindelin et al., 2012). Morphological parameters (Table 1) were extracted to determine how the different segmentation approaches affect the volume, length and structural complexity of the pore and organic phases.

The 3D architecture of the sample was visualized using the volume rendering software Drishti (Limaye, 2012). In order to compare this 3D rendering with the actual sample, and check that the root and pore elements visible to the naked eye are correctly identified, the core was cut open with a serrated knife along a pre-marked section one day after scanning. Using a prior marking (either an incision in the PVC tube or a piece of metal, both of which will be visible in the X-ray attenuation coefficients), the equivalent vertical section was located in the segmented volume and overlain with a high-resolution photograph of the cut-off face. While there is no infallible way of cutting open a core without causing disturbance, the cohesive nature of the clay means that the largest pore structures and the position of the roots are likely to be preserved.

3. Results

3.1. Quality control of the segmentation method

Observation of the segmented horizontal slices provides insight into the different types of pores and organic matter elements detected by our segmentation method (Fig. 6). The larger organic elements have a complex inner structure with a hollow center and multiple other internal voids: these air spaces within roots and stems (aerenchyma) are an adaptation strategy of coastal wetland plants such as *Spartina* to anoxic conditions (Mitsch & Gosselink, 1986). The smaller, tubular root elements visible in the Z-slice correspond either to lateral roots branching off from the main *Spartina* root system, or to the roots of other plant species present on site such as *Atriplex or Puccinellia*. The porosity elements appear either as tubular features, corresponding to inner voids within roots and voids left behind by decaying roots, or as patches with no organic origin.
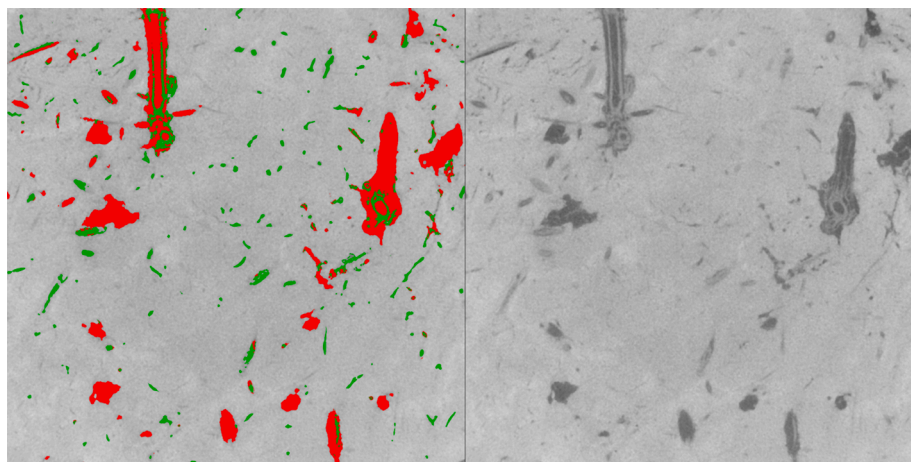
Fig. 6. Segmentation example, showing the pore phase in red and the organic matter phase in green overlain over the remaining inorganic phase. (For interpretation of the references to color in this figure legend, the reader is referred to the web version of this article.)

Adding the Frangi filter had no visible effect on the detection of pore elements, but considerably increased the size, extent and complexity of the organic matter phase (Fig. 7). At NFF5000 the organic matter phase is limited to areas connected to large pores: because of the hysteresis thresholding applied, medium grayscale voxels are only segmented if they are connected to a low grayscale voxel. Therefore the Frangi filter is particularly efficient at detecting thin unconnected root elements with no internal voids. By contrast, changing the noise removal threshold from 5,000 to 2,500 voxels had little visible impact on the 3D volumes of either the pore or the organic matter phases (Fig. 7).

Ground referencing shows that the segmentation method proposed successfully distinguishes areas dominated by roots from areas dominated by pores (Fig. 8). On the high resolution photograph, the top half of the cut face (0–6 cm) is pockmarked by small roots, though individual roots are difficult to visualize except for a few of the larger *Spartina* roots. The section between 6 and 12 cm contains more and larger porosity elements; the structure and distribution of these pores are also similar to what is observed on the segmented volume.

3.2. Quantification and distinction between live roots and necromass

The segmented pore phase can be separated into three regions: 0–6 cm, 6–10 cm and 10–14 cm. The first region at 0–6 cm is characterized by a low pore fraction and bulk volume, a low connectivity, but a peak in both the pores and organic matter' skeleton length (Figs. 9-10). This is due to the influence of the *Spartina* stem and roots, which contain several transport pathways and unconnected hollow chambers that add to the length of the overall pore system. The second region at 6–10 cm sees a peak in the pore fraction (Fig. 9) and in the connectedness and complexity of the pore system (Fig. 10). This region coincides with the branching off of the main *Spartina* root into lateral roots at about 8 cm, and with a horizontal crack visible in the rendered volume (Fig. 7). The root system may have preferentially developed within an area of structural fragility and lesser density, as has been observed in previous studies (Lucas et al., 2019). The third region sees a slight decrease in the bulk volume, connectedness and complexity of the pore system (Figs. 9-10).

The organic matter phase is dense throughout the 15 cm sample (Fig. 7), which is to be expected as we are still within the root zone of a biologically diverse upper saltmarsh: the saltmarsh root zone extends from 15 to 50 cm depending on plant species and environmental conditions (De Baets et al., 2008). The organic phase is denser in the first 5 cm then starts to decrease downcore (Fig. 9). Adding the Frangi filter leads to the detection of a larger and more complex organic matter phase overall, with a higher fraction, bulk volume and total skeleton length

detected at all depths (Figs. 9-10). Adding the Frangi filter also highlights the downcore decrease of the organic fraction (Fig. 9), notably by detecting a higher number of elements not connected to the main root system: in the first 5 cm of the sample, 25% of all segmented elements are connected to the main root feature in FF5000 and FF2500, against 50% for NFF5000 (Fig. 10).

Fig. 11 shows the potential of the Frangi filter to detect the necromass as well as the surface-connected live root system. The live root phase highlights one large *Spartina* root that branches out into smaller horizontal roots at about 80 mm depth. The live root system detected using the Frangi filter is larger and more complex, with a greater bulk volume and number of branches in the skeleton, and reaches 2.5 cm deeper. A number of thin lateral roots also becomes apparent. Without the Frangi filter, by contrast, the live root system appears fragmented, and very little of the necromass is detected.

4. Discussion

The use of µCT in soil sciences allows us to visualize and quantify crucial structures and processes in the subsurface environment, but this technology presents ongoing challenges: sampling procedures to minimize sediment disturbance remain time-consuming, access to specialist X-ray µCT scanning equipment is still not widespread in the soil science community, and the large datasets can create issues with processing and data storage. Finally, until standard segmentation methods are widely agreed upon, interpretation of the µCT volumes will require specific expertise in 3D signal processing and image analysis. Therefore multidisciplinary methodology papers are necessary to disseminate novel image processing techniques and encourage the wider use of µCT by soil scientists.

The approach outlined in this paper has multiple potential applications for soil science. The three-phase segmentation (pores, organic matter elements, sediment matrix) allows the study of pore-root interactions, something which has so far only been attempted in simplified conditions such as sieved and repacked soil columns (Lucas et al., 2019). These interactions are expected to play an important role in natural soil structure because of the high trait plasticity of roots: their growth depends on the distribution of water, nutrients and of the areas of least resistance marked by the porosity elements (Bardgett et al., 2014). At a higher resolution, the method could be used to study the internal structure of plants and roots to visualize internal air spaces and infer nutrient and fluid exchanges between the surface and subsurface: the presence of aerenchyma has been an obstacle in previous segmentation attempts using a visual tracking algorithm (Zappala et al., 2013). In addition, the capacity of our method to distinguish live roots from the
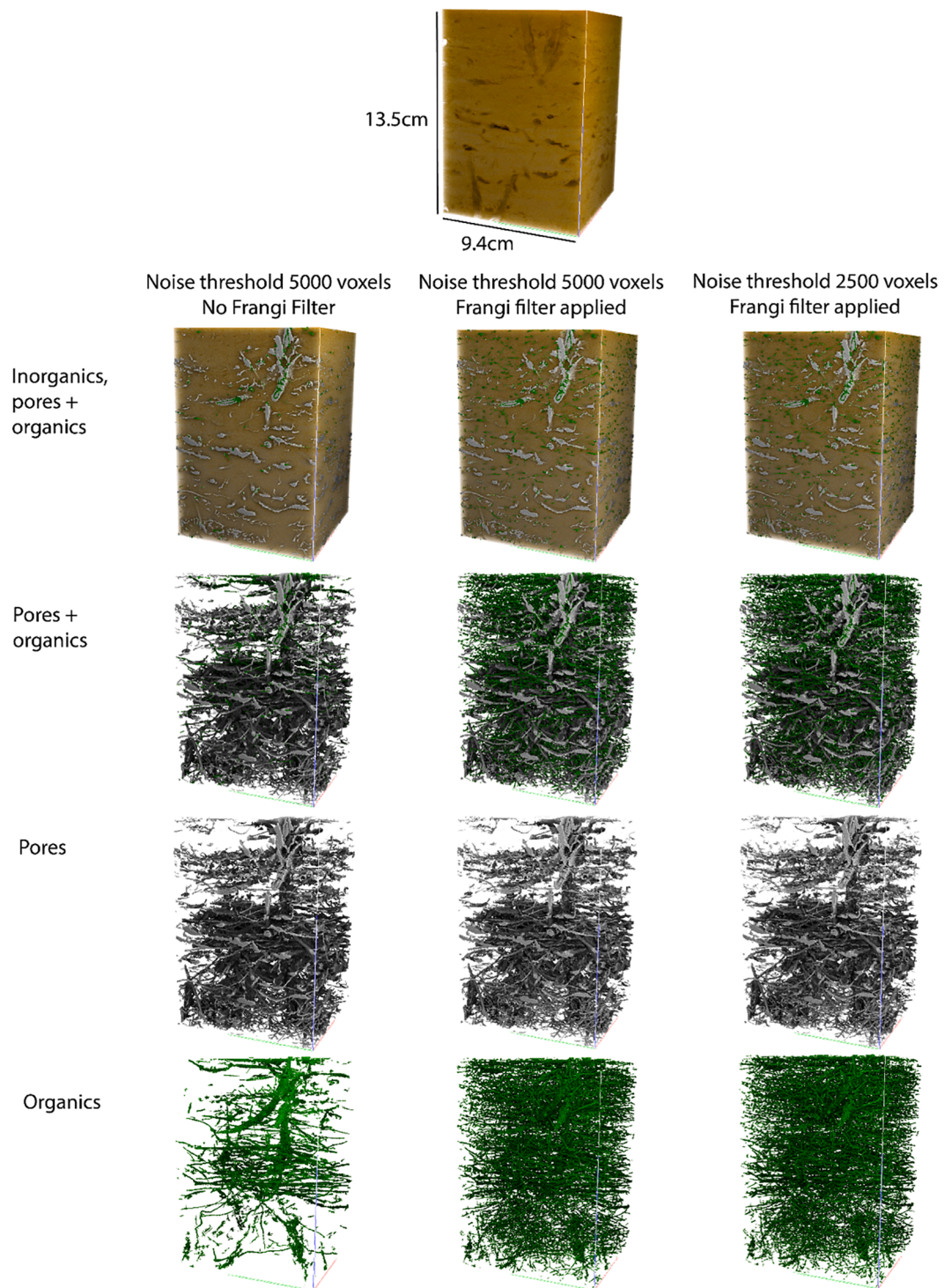
Fig. 7. Segmented volume visualization using different segmentation methods and noise thresholds. Grey = pores; green = organic matter; brown = inorganic matter. Volumes obtained using Drishti (Limaye, 2012). (For interpretation of the references to color in this figure legend, the reader is referred to the web version of this article.)
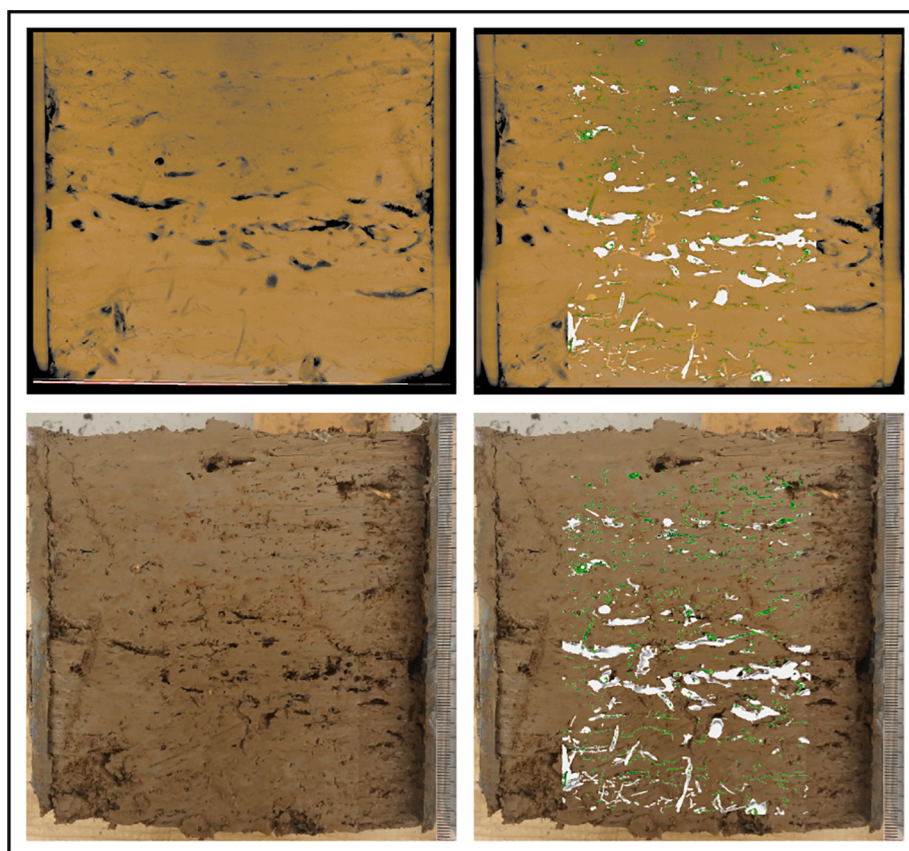
Fig. 8. Ground referencing using the segmented volume overlain over a photograph of the cut-off face of the core. On the segmented volume: brown = inorganic matter; grey = pores; green = organic matter. Volume obtained using Drishti. (For interpretation of the references to color in this figure legend, the reader is referred to the web version of this article.)

necromass opens the door for μCT applications to the study of soil structural stability. Indeed, roots can have either a weakening or a stabilizing effect on the soil depending on their structure, connectedness and state of decay (Brooks et al., 2020). Coarse roots can dislodge sediment and contribute to cliff-face erosion (Feagin et al., 2009), while thinner and denser root meshes hold the soil together and provide a physical barrier between the sediment and the water (Brooks et al., 2020; Gedan et al., 2011). Decaying unconnected roots also contribute to making the soil less dense and more cohesive (Brooks et al., 2020; Feagin et al., 2009).

Finally, the proposed method opens the door to the study of soil carbon dynamics and greenhouse gas exchanges in various types of soils. The potential of μCT to model gas exchanges within 3D macropore structures is already known (van Marcke et al., 2010). Our approach can further the state of knowledge by providing a robust way of estimating root biomass. This should improve the estimation of carbon stocks since root systems and particularly the fine-root mass contribute disproportionately to soil carbon sequestration compared to the aboveground part of the plant (He et al., 2018). Root biomass estimation still lacks a methodological consensus (Addo-Danso et al., 2016), and traditional methods of belowground biomass estimation rely on labor-intensive and time-consuming destructive sampling protocols, as highlighted by Valiela (2015): "This project became legendary as the most tedious task

in our labs, tolerated only by everyone taking turns at the detailed and nearly endless staining, sorting, drying, and weighing protocols". Furthermore, distinguishing live roots from necromass is recommended when estimating carbon sequestration potential in the soil (Adame et al., 2017). The proposed method, based on the connection of the root system to the surface, comes with its own limitations: the minimal size of roots detected depends on the scanning resolution chosen, and live root systems connected to shoots outside the perimeter of the core will be detected as necromass; prior knowledge of the live root thickness, internal structure and architecture is recommended to choose appropriate scanning parameters and to interpret the μCT volumes. Nevertheless, owing to the capacity of μCT to rapidly and non-destructively segment large and complex root systems, the method outlined in this paper could play a crucial role in studies of soil carbon dynamics.

5. Conclusion

This study applied X-ray Computed Microtomography to a highly heterogenous saltmarsh sediment core. We developed a hybrid segmentation method that combines local adaptive thresholding and shape detection to visualize and quantify the 3D distribution of pores, live roots and necromass. The segmented volumes of roots and pores closely match the structures observed on high-resolution photographs of the
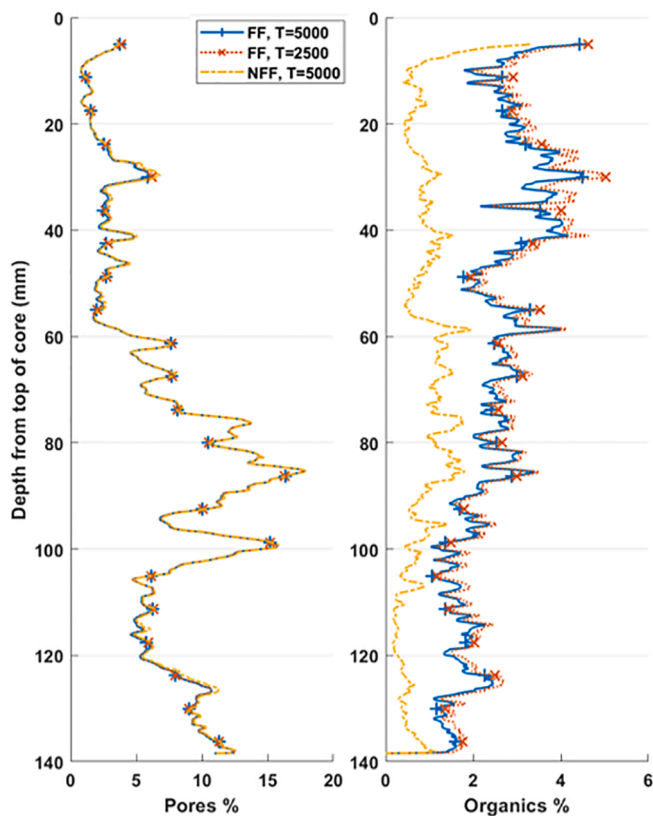
Fig. 9. Depth profiles of the fractions of pores and of organic matter within the segmented volume. FF: Frangi filter applied; NFF: No Frangi filter applied. T = 5000: Noise threshold set at 5,000 voxels; T = 2,500: Noise threshold set at 2,500 voxels.

core taken along a cut-off face. We find that the use of a Frangi filter for tubular structure enhancement is particularly efficient to highlight fine root elements that have a low density contrast with the mineral phase. Compared with region-growth segmentation methods, which only segment objects connected to pre-selected seed points, this method is more versatile because it requires no prior knowledge of the core content, and because it distinguishes between the live root system and the necromass. Our analysis of the pore and organic matter elements' volume and structure shows clear interactions between the two phases: root decay is a source of porosity in the sediment, while the presence of areas of lower density with a higher concentration of pores determine where roots are able to develop. Our application of X-ray µCT has the potential to provide unprecedented knowledge of the 3D organisation of pores and organic matter within heterogeneous soils, and to explore key ecosystem functioning such as erodibility and carbon sequestration dynamics.

Author contributions

The manuscript was written through contributions of all authors. All authors have given approval to the final version of the manuscript. Iris Moeller secured funding for the RESIST project and defined our research objectives. Kate Spencer and Simon Carr developed an initial workflow for X-ray µCT application to saltmarsh soils. Clementine Chirol collected the sample with field assistance from all authors, processed the dataset using an enhanced workflow and wrote the article with edits from all authors.

Declaration of Competing Interest

The authors declare that they have no known competing financial interests or personal relationships that could have appeared to influence the work reported in this paper.
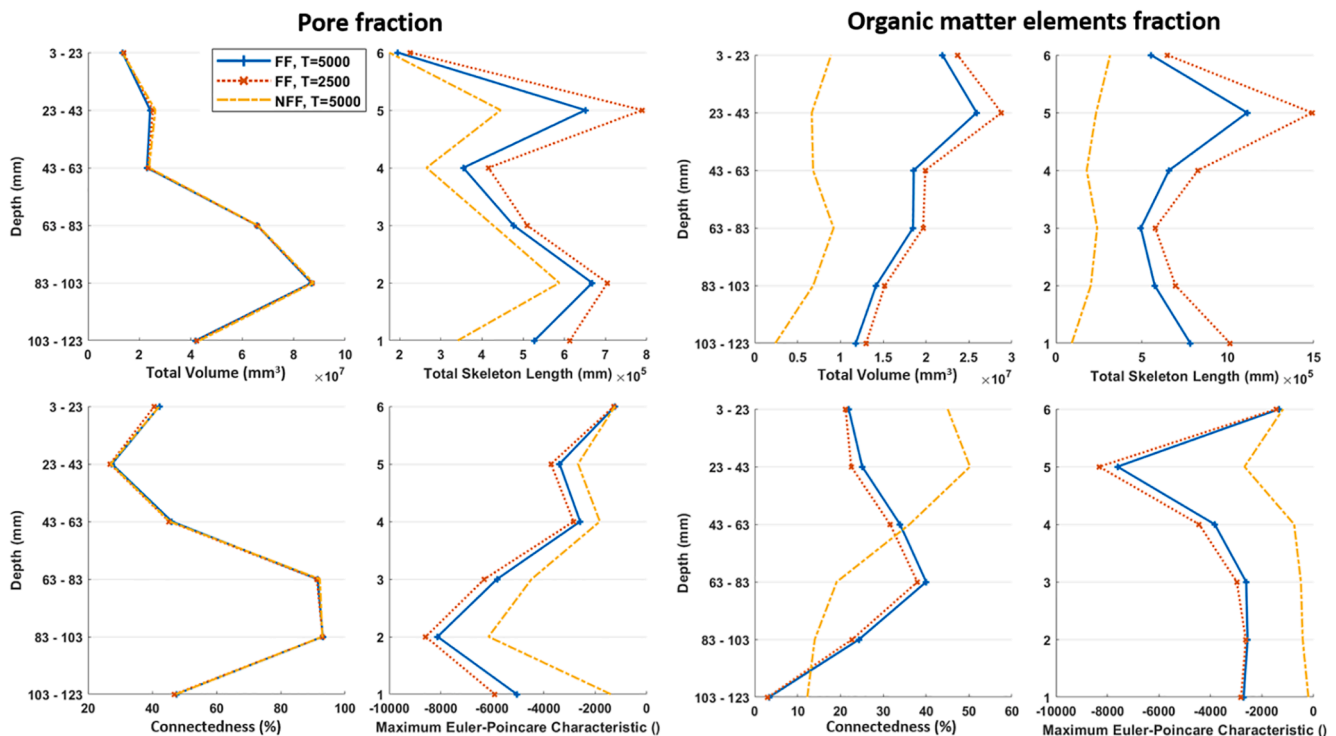

Fig. 10. Topological analysis of pores and organic matter in 2-cm sections using BoneJ. () stands for no unit.
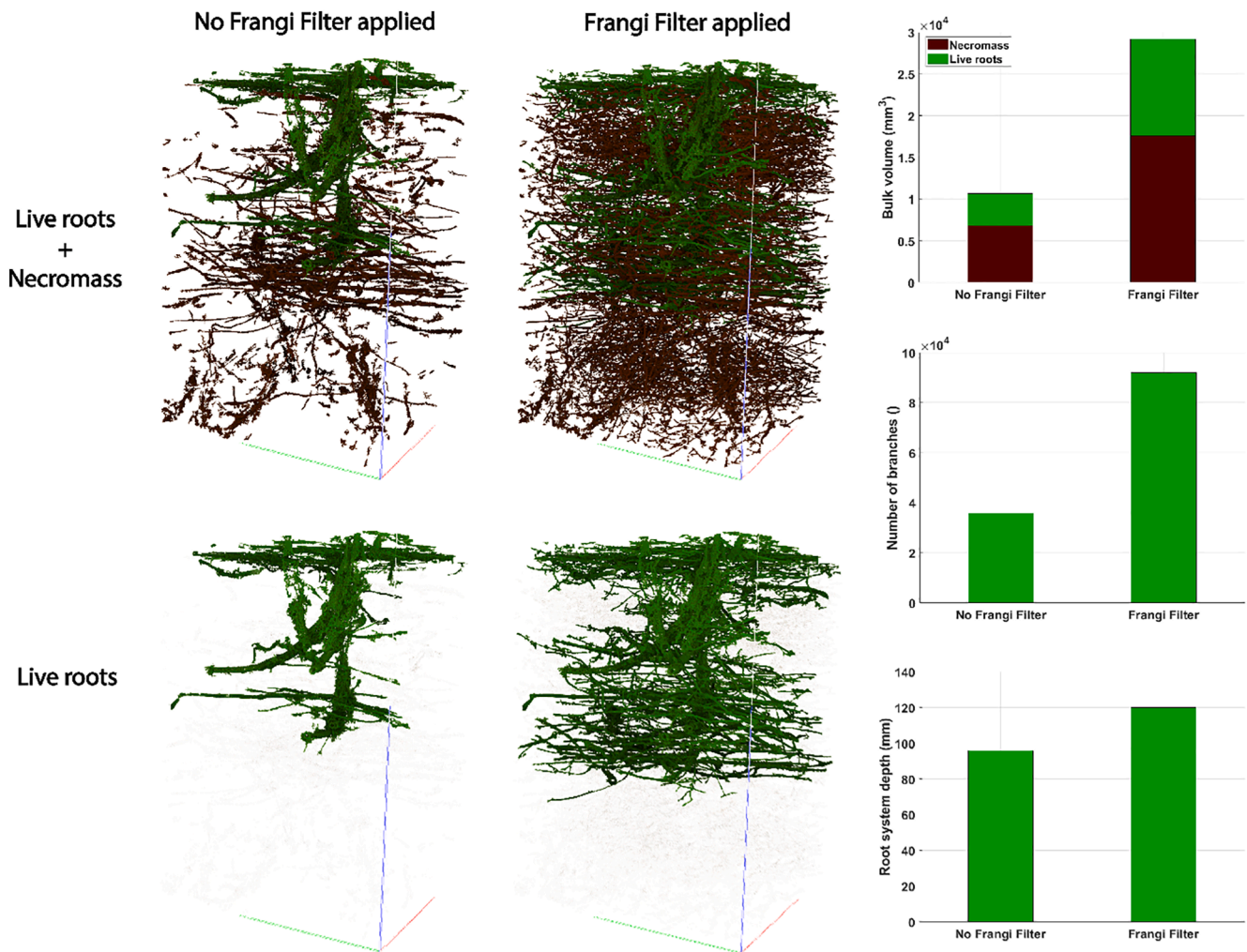
Fig. 11. Effect of the Frangi filter on the extent, bulk volume, number of branches and root system depth of surface-connected "live" roots (green) and on the bulk volume of the necromass (dark red). The noise threshold is 5000 voxels. (For interpretation of the references to color in this figure legend, the reader is referred to the web version of this article.)

References

Adame, M.F., Cherian, S., Reef, R., Stewart-Koster, B., 2017. Mangrove root biomass and the uncertainty of belowground carbon estimations. For. Ecol. Manage. 403, 52–60. https://doi.org/10.1016/j.foreco.2017.08.016.

Addo-Danso, S.D., Prescott, C.E., Smith, A.R., 2016. Methods for estimating root biomass and production in forest and woodland ecosystem carbon studies: A review. For. Ecol. Manage. 359, 332–351. https://doi.org/10.1016/j.foreco.2015.08.015.

Ball, B.C., 2013. Soil structure and greenhouse gas emissions: A synthesis of 20 years of experimentation. Eur. J. Soil Sci. 64 (3), 357–373. https://doi.org/10.1111/ejss.12013.

Bardgett, R.D., Mommer, L., De Vries, F.T., 2014. Going underground: root traits as drivers of ecosystem processes. Trends Ecol. Evol. 29 (12), 692–699. https://doi.org/10.1016/j.tree.2014.10.006.

Bartholdy, J., Pedersen, J.B.T., Bartholdy, A.T., 2010. Autocompaction of shallow silty salt marsh clay. Sed. Geol. 223 (3–4), 310–319. https://doi.org/10.1016/j.sedgeo.2009.11.016.

Bendle, J.M., Palmer, A.P., Carr, S.J., 2015. A comparison of micro-CT and thin section analysis of Lateglacial glaciolacustrine varves from Glen Roy, Scotland. Quat. Sci. Rev. 114, 61–77. https://doi.org/10.1016/j.quascirev.2015.02.008.

Blagodatsky, S., Smith, P., 2012. Soil physics meets soil biology: Towards better mechanistic prediction of greenhouse gas emissions from soil. Soil Biol. Biochem. 47, 78–92. https://doi.org/10.1016/j.soilbio.2011.12.015.

Bradley, P., Morris, J., 1990. Physical characteristics of salt marsh sediments: ecological implications. Mar. Ecol. Prog. Ser. 61, 245–252. https://doi.org/10.3354/meps061245.

Brooks, H., Möller, I., Carr, S.J., Chirol, C., Christie, E., Evans, B., Spencer, K.L., Spencer, T., Royse, K., 2020. Resistance of salt marsh substrates to near-instantaneous hydrodynamic forcing. Earth Surf. Proc. Land. https://doi.org/10.1002/esp.4912.

Canny, J. (1986). A Computational Approach to Edge Detection. IEEE Transactions on Pattern Analysis and Machine Intelligence, PAMI-8(6), 679–698. https://doi.org/10.1109/ASICON.2011.6157287.

Carlson, W.D., 2006. Three-dimensional imaging of earth and planetary materials. Earth Planet. Sci. Lett. 249, 133–147. https://doi.org/10.1016/j.epsl.2006.06.020.

Carr, S.J., Diggens, L.M., Spencer, K.L., 2020. There is no such thing as 'undisturbed' soil and sediment sampling: sampler-induced deformation of salt marsh sediments revealed by 3D X-ray computed tomography. J. Soils Sedim. 20 (7), 2960–2976. https://doi.org/10.1007/s11368-020-02655-7.

Cnudde, V., Boone, M.N., 2013. High-resolution X-ray computed tomography in geosciences: A review of the current technology and applications. Earth Sci. Rev. 123, 1–17. https://doi.org/10.1016/j.earscirev.2013.04.003.

Corenblit, D., Baas, A.C.W., Bornette, G., Darrozes, J., Delmotte, S., Francis, R.A., Gurnell, A.M., Julien, F., Naiman, R.J., Steiger, J., 2011. Earth-Science Reviews Feedbacks between geomorphology and biota controlling Earth surface processes and landforms : A review of foundation concepts and current understandings. Earth-Sci. Rev. 106 (3–4), 307–331. https://doi.org/10.1016/j.earscirev.2011.03.002.

Dale, J., Cundy, A.B., Spencer, K.L., Carr, S.J., Croudace, I.W., Burgess, H.M., Nash, D.J., 2019. Sediment structure and physicochemical changes following tidal inundation at a large open coast managed realignment site. Sci. Total Environ. 660, 1419–1432. https://doi.org/10.1016/j.scitotenv.2018.12.323.

De Baets, S., Poesen, J., Reubens, B., Wemans, K., De Baerdemaeker, J., Muys, B., 2008. Root tensile strength and root distribution of typical Mediterranean plant species and their contribution to soil shear strength. Plant Soil 305 (1–2), 207–226. https://doi.org/10.1007/s11104-008-9553-0.

De Battisti, D., Fowler, M.S., Jenkins, S.R., Skov, M.W., Rossi, M., Bouma, T.J., Neyland, P.J., Griffin, J.N., 2019. Intraspecific Root Trait Variability Along Environmental Gradients Affects Salt Marsh Resistance to Lateral Erosion. Frontiers in Ecology and Evolution 7, 1–11. https://doi.org/10.3389/fevo.2019.00150.

Doube, M., Kłosowski, M.M., Arganda-carreras, I., Fabrice, P., 2010. UKPMC Funders Group BoneJ : free and extensible bone image analysis in ImageJ. Bone 47 (6), 1076–1079. https://doi.org/10.1016/j.bone.2010.08.023.BoneJ.

Dyer, K.R., 1995. Sediment transport processes in estuaries. Geomorphology and Sedimentology of Estuaries. Dev. Sedimentol. 53, 423–449. https://doi.org/10.1016/S0070-4571(05)80034-2.

Feagin, R. A., Lozada-Bernard, S. M., Ravens, T. M., Möller, I., Yeager, K. M., & Baird, A. H. (2009). Does vegetation prevent wave erosion of salt marsh edges? Proceedings of the National Academy of Sciences of the United States of America, 106(25), 10109–10113. https://doi.org/10.1073/pnas.0901297106.

Fonseca, J., O'Sullivan, C., Coop, M.R., Lee, P.D., 2013. Quantifying the evolution of soil fabric during shearing using scalar parameters. Geotechnique 63 (10), 818–829. https://doi.org/10.1680/geot.11.P.150.

Ford, H., Garbutt, A., & Skov, M. (2016). Coastal Biodiversity and Ecosystem Service Sustainability (CBESS) percentage cover of plant species on salt marsh sites at Morecambe Bay and Essex. https://doi.org/https://doi.org/10.5285/90bdf4ff-03d9-4aa4-bcad-5139863ab188.

Frangi, A. F., Niessen, W. J., Vincken, K. L., & Viergever, M. A. (1998). Multiscale vessel enhancement filtering. International Conference on Medical Image Computing and Computer-Assisted Intervention, 130–137. https://doi.org/10.1007/BFb0056195.

French, J., 2006. Tidal marsh sedimentation and resilience to environmental change: Exploratory modelling of tidal, sea-level and sediment supply forcing in predominantly allochthonous systems. Marine Geology, 235(1–4 SPEC. ISS.), 119–136. https://doi.org/10.1016/j.margeo.2006.10.009.

Gao, W., Schlüter, S., Blaser, S.R.G.A., Shen, J., Vetterlein, D., 2019. A shape-based method for automatic and rapid segmentation of roots in soil from X-ray computed tomography images: Rootine. Plant Soil 441 (1–2), 643–655. https://doi.org/10.1007/s11104-019-04053-6.

Gedan, K.B., Kirwan, M.L., Wolanski, E., Barbier, E.B., Silliman, B.R., 2011. The present and future role of coastal wetland vegetation in protecting shorelines: Answering recent challenges to the paradigm. Climatic Change (Vol. 106 (1), 7–29. https://doi.org/10.1007/s10584-010-0003-7.

Gharedaghloo, B., Price, J.S., Rezanezhad, F., Quinton, W.L., 2018. Evaluating the hydraulic and transport properties of peat soil using pore network modeling and X-ray micro computed tomography. J. Hydrol. 561, 494–508. https://doi.org/10.1016/j.jhydrol.2018.04.007.

Griggs, A.J., Davies, S.M., Abbott, P.M., Coleman, M., Palmer, A.P., Rasmussen, T.L., Johnston, R., 2015. Visualising tephra sedimentation processes in the marine environment: The potential of X-ray microtomography. Geochem. Geophys. Geosyst. 16, 4329–4343. https://doi.org/10.1002/2015GC006073.Received.

He, Z., Peng, Y., Guan, D., Hu, Z., Chen, Y., Lee, S.Y., 2018. Appearance can be deceptive: shrubby native mangrove species contributes more to soil carbon sequestration than fast-growing exotic species. Plant Soil 432 (1–2), 425–436. https://doi.org/10.1007/s11104-018-3821-4.

Helliwell, J.R., Sturrock, C.J., Grayling, K.M., Tracy, S.R., Flavel, R.J., Young, I.M., Whalley, W.R., Mooney, S.J., 2013. Applications of X-ray computed tomography for examining biophysical interactions and structural development in soil systems: A review. Eur. J. Soil Sci. 64 (3), 279–297. https://doi.org/10.1111/ejss.12028.

Houston, A.N., Schmidt, S., Tarquis, A.M., Otten, W., Baveye, P.C., Hapca, S.M., 2013. Effect of scanning and image reconstruction settings in X-ray computed microtomography on quality and segmentation of 3D soil images. Geoderma 207–208 (1), 154–165. https://doi.org/10.1016/j.geoderma.2013.05.017.

Hvorslev, M. J. (1949). Subsurface exploration and sampling of soils for civil engineering purposes. Waterways Experiment Station, Vicksburg.

Kaestner, A., Schneebeli, M., Graf, F., 2006. Visualizing three-dimensional root networks using computed tomography. Geoderma 136 (1–2), 459–469. https://doi.org/10.1016/j.geoderma.2006.04.009.

Keller, T., Lamandé, M., Peth, S., Berli, M., Delenne, J.Y., Baumgarten, W., Rabbel, W., Radjaï, F., Rajchenbach, J., Selvadurai, A.P.S., Or, D., 2013. An interdisciplinary approach towards improved understanding of soil deformation during compaction. Soil Tillage Res. 128, 61–80. https://doi.org/10.1016/j.still.2012.10.004.

Ketcham, R.A., 2005. Three-dimensional grain fabric measurements using high-resolution X-ray computed tomography. J. Struct. Geol. 27, 1217–1228. https://doi.org/10.1016/j.jsg.2005.02.006.

Ketcham, R.A., Carlson, W.D., 2001. Acquisition, optimization and interpretation of x-ray computed tomographic imagery: Applications to the geosciences. Comput. Geosci. 27 (4), 381–400. https://doi.org/10.1016/S0098-3004(00)00116-3.

Kroon, D.-J. (2010). Hessian based Frangi Vesselness filter (https://www.mathworks.com/matlabcentral/fileexchange/24409-hessian-based-frangi-vesselness-filter), MATLAB Central File Exchange.

Limaye, A. (2012). Drishti: a volume exploration and presentation tool. 85060X. https://doi.org/10.1117/12.935640.

Lin, H., 2010. Earth's Critical Zone and hydropedology: Concepts, characteristics, and advances. Hydrol. Earth Syst. Sci. 14 (1), 25–45. https://doi.org/10.5194/hess-14-25-2010.

Lucas, M., Schlüter, S., Vogel, H.J., Vetterlein, D., 2019. Roots compact the surrounding soil depending on the structures they encounter. Sci. Rep. 9 (1), 1–13. https://doi.org/10.1038/s41598-019-52665-w.

Mairhofer, S., Zappala, S., Tracy, S.R., Sturrock, C., Bennett, M., Mooney, S.J., Pridmore, T., 2012. RooTrak : Automated Recovery of Three-Dimensional Plant Root Architecture in Soil from X-Ray Microcomputed Tomography Images Using Visual Tracking. Plant Physiol. 158, 561–569. https://doi.org/10.1104/pp.111.186221.

Menon, M., Mawodza, T., Rabbani, A., Blaud, A., Lair, G.J., Babaei, M., Kercheva, M., Rousseva, S., Banwart, S., 2020. Pore system characteristics of soil aggregates and their relevance to aggregate stability. Geoderma 366. https://doi.org/10.1016/j.geoderma.2020.114259.

Menzies, J., van der Meer, J.J.M., Ravier, E., 2016. A kinematic unifying theory of microstructures in subglacial tills. Sed. Geol. 344, 57–70. https://doi.org/10.1016/j.sedgeo.2016.03.024.

Mitsch, W. J., & Gosselink, J. G. (1986). Wetlands (p. 539). Van Nostrand Reinhold, NY.

Moffett, K.B., Gorelick, S.M., McLaren, R.G., Sudicky, E.A., 2012. Salt marsh ecohydrological zonation due to heterogeneous vegetation-groundwater-surface water interactions. Water Resour. Res. 48 (2) https://doi.org/10.1029/2011WR010874.

Mooney, S.J., 2002. Three-dimensional visualization and quantification of soil macroporosity and water flow patterns using computed tomography. Soil Use Manag. 18 (2), 142–151. https://doi.org/10.1079/SUM2002121.

Naveed, M., Herath, L., Moldrup, P., Arthur, E., Nicolaisen, M., Norgaard, T., Ferré, T.P. A., de Jonge, L.W., 2016. Spatial variability of microbial richness and diversity and relationships with soil organic carbon, texture and structure across an agricultural field. Appl. Soil Ecol. 103, 44–55. https://doi.org/10.1016/j.apsoil.2016.03.004.

Ngom, N.F., Garnier, P., Monga, O., Peth, S., 2011. Extraction of three-dimensional soil pore space from microtomography images using a geometrical approach. Geoderma 163 (1–2), 127–134. https://doi.org/10.1016/j.geoderma.2011.04.013.

Pedersen, L.L., Smets, B.F., Dechesne, A., 2015. Measuring biogeochemical heterogeneity at the micro scale in soils and sediments. Soil Biol. Biochem. 90, 122–138. https://doi.org/10.1016/j.soilbio.2015.08.003.

Persson, H.A., 2012. The High Input of Soil Organic Matter from Dead Tree Fine Roots into the Forest Soil. International Journal OfForestry Research 2012. https://doi.org/10.1155/2012/217402.

Pezeshki, S.R., DeLaune, R.D., 2012. Soil Oxidation-Reduction in Wetlands and Its Impact on Plant Functioning. Biology 1 (3), 196–221. https://doi.org/10.3390/biology1020196.

Phillips, E.R., Evans, D.J.A.E., van der Meer, J.J.M., Lee, J.R., 2018. Microscale evidence of liquefaction and its potential triggers during soft-bed deformation within subglacial traction tills. Quaternary Science Review 181, 123–143.

Pöhlitz, J., Rücknagel, J., Koblenz, B., Schlüter, S., Vogel, H.J., Christen, O., 2018. Computed tomography and soil physical measurements of compaction behaviour under strip tillage, mulch tillage and no tillage. Soil Tillage Res. 175, 205–216. https://doi.org/10.1016/j.still.2017.09.007.

Pot, V., Zhong, X., Baveye, P.C., 2020. Effect of resolution, reconstruction settings, and segmentation methods on the numerical calculation of saturated soil hydraulic conductivity from 3D computed tomography images. Geoderma 362. https://doi.org/10.1016/j.geoderma.2019.114089.

Rabot, E., Wiesmeier, M., Schlüter, S., Vogel, H.J., 2018. Soil structure as an indicator of soil functions: A review. Geoderma 314, 122–137. https://doi.org/10.1016/j.geoderma.2017.11.009.

Ray, A. (2011). CT pro user manual. Nikon Metrology, Hertfordshire, England.

Rogers, E.D., Benfey, P.N., 2015. Regulation of plant root system architecture: Implications for crop advancement. Curr. Opin. Biotechnol. 32, 93–98. https://doi.org/10.1016/j.copbio.2014.11.015.

Rogers, E.D., Monaenkova, D., Mijar, M., Nori, A., Goldman, D.I., Benfey, P.N., 2016. X-ray computed tomography reveals the response of root system architecture to soil texture. Plant Physiol. 171 (3), 2028–2040. https://doi.org/10.1104/pp.16.00397.

Schindelin, J., Arganda-Carreras, I., Frise, E., Kaynig, V., Longair, M., Pietzsch, T., Preibisch, S., Rueden, C., Saalfeld, S., Schmid, B., Tinevez, J.Y., White, D.J., Hartenstein, V., Eliceiri, K., Tomancak, P., Cardona, A., 2012. Fiji: An open-source platform for biological-image analysis. Nat. Methods 9 (7), 676–682. https://doi.org/10.1038/nmeth.2019.

Schlüter, S., Weller, U., Vogel, H.J., 2010. Segmentation of X-ray microtomography images of soil using gradient masks. Comput. Geosci. 36 (10), 1246–1251. https://doi.org/10.1016/j.cageo.2010.02.007.

Schulz, H., Postma, J. A., van Dusschoten, D., Scharr, H., & Behnke, S. (2013). Plant Root System Analysis from MRI Images. Communications in Computer and Information Science, 359 CCIS, 411–425. https://doi.org/10.1007/978-3-642-38241-3_28.

Smith, K.A., Ball, T., Conen, F., Dobbie, K.E., Massheder, J., Rey, A., 2003. Exchange of greenhouse gases between soil and atmosphere. Eur. J. Soil Sci. 54, 779–791. https://doi.org/10.1046/j.1365-2389.2003.00567.x.

Spagnolo, M., Phillips, E., Piotrowski, J.A., Rea, B.R., Clark, C.D., Stokes, C.R., Carr, S.J., Ely, J.C., Ribolini, A., Wysota, W., Szuman, I., 2016. Ice stream motion facilitated by a shallow-deforming and accreting bed. Nat. Commun. 7, 1–11. https://doi.org/10.1038/ncomms10723.

Spencer, K.L., Carr, S.J., Diggens, L.M., Tempest, J.A., Morris, M.A., Harvey, G.L., 2017. The impact of pre-restoration land-use and disturbance on sediment structure, hydrology and the sediment geochemical environment in restored saltmarshes. Sci. Total Environ. 587–588, 47–58. https://doi.org/10.1016/j.scitotenv.2016.11.032.

Swanson, S., Kozlowski, D., Hall, R., Heggem, D., Lin, J., 2017. Riparian proper functioning condition assessment to improve watershed management for water quality. J. Soil Water Conserv. 72 (2), 168–182. https://doi.org/10.1016/j.hal.2017.06.001.Submit.

Taina, I.A., Heck, R.J., Elliot, T.R., 2008. Application of X-ray computed tomography to soil science: A literature review. Can. J. Soil Sci. 88 (1), 1–19. https://doi.org/10.4141/CJSS06027.

Tarplee, M.F.V., van der Meer, J.J.M., Davis, G.R., 2011. The 3D microscopic "signature" of strain within glacial sediments revealed using X-ray computed microtomography. Quat. Sci. Rev. 30 (23–24), 3501–3532. https://doi.org/10.1016/j.quascirev.2011.05.016.

Teixeira, A., Duarte, B., & Caçador, I. (2014). Salt Marshes and Biodiversity. In Sabkha Ecosystems: Volume IV: Cash Crop Halophyte and Biodiversity Conservation (Vol. 47, pp. 283–298). https://doi.org/10.1007/978-94-007-7411-7.

Turner, R.E., 2004. Coastal wetland subsidence arising from local hydrologic manipulations. Estuaries 27 (2), 265–272. https://doi.org/10.1007/BF02803383.

Valiela, I., 2015. The Great Sippewissett Salt Marsh Plots—Some History, Highlights, and Contrails from a Long-Term Study. Estuaries Coasts 38, 1099–1120. https://doi.org/10.1007/s12237-015-9976-9.

van Marcke, P., Verleye, B., Carmeliet, J., Roose, D., Swennen, R., 2010. An Improved Pore Network Model for the Computation of the Saturated Permeability of Porous Rock. Transp. Porous Media 85 (2), 451–476. https://doi.org/10.1007/s11242-010-9572-1.

Voepel, H., Leyland, J., Hodge, R.A., Ahmed, S., Sear, D., 2019. Development of a vector-based 3D grain entrainment model with application to X-ray computed tomography scanned riverbed sediment. Earth Surf. Proc. Land. 44 (15), 3057–3077. https://doi.org/10.1002/esp.4608.

Wildenschild, D., Sheppard, A.P., 2013. X-ray imaging and analysis techniques for quantifying pore-scale structure and processes in subsurface porous medium systems. Adv. Water Resour. 51, 217–246. https://doi.org/10.1016/j.advwatres.2012.07.018.

Xiong, Y., Ola, A., Phan, S.M., Wu, J., Lovelock, C.E., 2019. Soil Structure and Its Relationship to Shallow Soil Subsidence in Coastal Wetlands. Estuaries Coasts 42 (8), 2114–2123. https://doi.org/10.1007/s12237-019-00659-2.

Young, D. (2014). Canny edge detection in 2-D and 3-D (https://www.mathworks.com/matlabcentral/fileexchange/45459-canny-edge-detection-in-2-d-and-3-d), MATLAB Central File Exchange.

Zappala, S., Mairhofer, S., Tracy, S., Sturrock, C.J., Bennett, M., Pridmore, T., Mooney, S.J., 2013. Quantifying the effect of soil moisture content on segmenting root system architecture in X-ray computed tomography images. Plant Soil 370 (1–2), 35–45. https://doi.org/10.1007/s11104-013-1596-1.